Study of flow separation over an airfoil with synthetic jet control using large-eddy simulation

By D. You AND P. Moin

1. Motivation and objectives

The performance and stability of an airplane is often degraded by flow separation. In recent years, control devices involving zero-net-mass-flux oscillatory jets or synthetic jets have shown good feasibility for industrial applications and effectiveness in controlling flow separation (Glezer & Amitay 2002; Rumsey *et al.* 2004; Wygnanski 2004). The application of synthetic jets to flow separation control is based on their ability to stabilize the boundary layer by adding/removing momentum to/from the boundary layer with the formation of vortical structures. The vortical structures in turn promote boundary layer mixing and hence momentum exchange between the outer and inner parts of the boundary layer. The control performance of the synthetic jets greatly relies on parameters such as the amplitude, frequency, and location of the actuation, and numerical simulations are especially suitable for an extensive parametric study to optimize the control parameters.

For numerical simulations, an accurate prediction, not to mention control, of the flow over an airfoil at a practical Reynolds number is a challenging task. The flow over an airfoil is inherently complex and exhibits a variety of physical phenomena including strong pressure gradients, flow separation, and confluence of boundary layers and wakes (Khorrami *et al.* 1999, 2000; Ying *et al.* 1998; Mathias *et al.* 1999). For prediction of such unsteady flows, large-eddy simulation (LES) is suitable because it provides detailed spatial and temporal information regarding a wide range of turbulence scales, which is precisely what is needed to gain better insight into the flow physics of this configuration.

Over the past decade, there have been several advances in large eddy simulation methodology for engineering analysis of complex flows. The most significant enabling technology has been in the development of robust, non-dissipative numerical methods for large-eddy simulation in complex configurations. To achieve robustness and numerical stability, the principle of discrete kinetic energy conservation has been incorporated in the numerical methodology. In this study, we employ such a kinetic-energy conservative LES solver to simulate flow separation over a NACA 0015 airfoil with and without synthetic-jet control at a high Reynolds number. Two different angles of attack 16.6° and 20° are considered where flow separates around a mid-chord location and near the leading edge, respectively. The unstructured-grid capability of the solver allows us to effectively handle the complex flow configuration involving an embedded synthetic-jet actuator and wind-tunnel walls.

The flow configuration and other computational parameters used for the present LES are described in Section 2. In Section 3, discussion of the simulation results, grid-refinment study, comparison against experimental data, and mechanism for synthetic-jet separation control are presented, and this is followed by conclusions in Section 4.
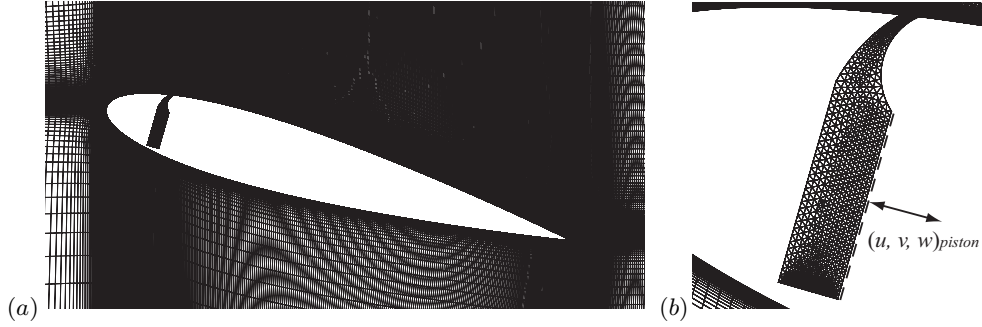
FIGURE 1. (*a*) Computational grid over a NACA 0015 airfoil and (*b*) unstructured-grid distribution inside the synthetic-jet actuator and definitions of the actuator boundary conditions in the case of 16.6° angle of attack.

2. Computational Details

2.1. *Flow configuration*

The flow configuration and the computational grid for study of active control of flow separation over an airfoil is shown in figure 1. This configuration was experimentally studied by Gilarranz *et al.* (2005). In the experiment, a NACA 0015 airfoil was installed in a wind tunnel. The slot of the actuator had a width of 0.53% chord across the entire length of the span and was placed at 12% chord location measured from the leading edge on the suction side of the airfoil. In the experiment, this location was selected to provide sufficient volume to accommodate the synthetic-jet actuator inside the airfoil.

The present study focuses on cases with angles of attack of 16.6° and 20°. As shown in figure 2, in the case of 16.6° angle of attack, flow separates from a mid-chord location of the airfoil in the uncontrolled case, and the control effect is most remarkable. In the case of 20° angle of attack, flow separates near the leading edge in the uncontrolled case, and the control effect is marginal. For these angles of attack, experimental data such as the mean surface pressure coefficients and wake profiles are available for comparison (Gilarranz *et al.* 2005).

The computational domain is of size $L_x \times L_y \times L_z = 6C \times 2.44C \times 0.2C$. In the present LES, a smaller domain size than that in the experiment is employed in the spanwise direction to reduce the computational cost. The Reynolds number of this flow is 8.96×10^5, based on the airfoil chord and inflow freestream velocity. In this study, it is important to precisely predict the flow through the synthetic-jet actuator because the directional variation of the jets during the oscillatory period greatly affects the boundary layer. Therefore, in the present study, the flow inside the actuator and resulting synthetic jets are simulated along with the external flow field using an unstructured-grid capability of the present LES solver. Figure 1(*b*) shows the synthetic-jet actuator modeled with an unstructured mesh. In the experiment, a piston engine is utilized to generate a sinusoidal mass flux and generates synthetic jets through the spanwise cavity slot. To mimic the oscillatory motion of a piston engine in the experiment, we apply sinusoidal velocity boundary conditions to a cavity side wall as shown in figure 1(*b*) and as follows:

$$(u_{piston}, v_{piston}, w_{piston})/U_\infty = (\cos(\alpha), -\sin(\alpha), 0)A_p \sin(2\pi ft), \qquad (2.1)$$

where α is the angle of attack, and 16.6° and 20° are considered. The frequency of the sinusoidal oscillation of the cavity side wall is $f = 1.284U_\infty/C$, which corresponds to 120Hz in the experiment of Gilarranz *et al.* (2005). A_p corresponds to the amplitude
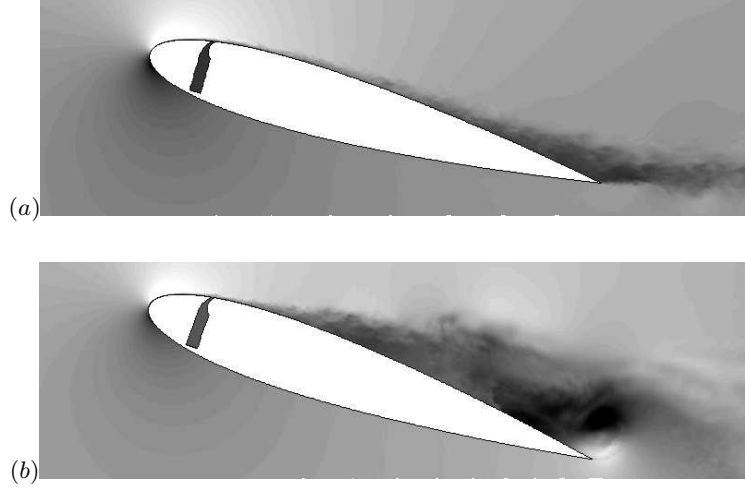
FIGURE 2. Contour plots of the instantaneous streamwise velocity over an airfoil. (*a*) Angle of attack 16.6°; (*b*) angle of attack 20°.

of oscillatory motion of the piston generating the peak bulk jet velocity at the cavity exit nozzle of $U_{max} = 2.14 U_\infty$. The same momentum coefficient as in the experiment is produced as:

$$C_\mu = \frac{h(\rho U_{max}^2)}{C(\rho U_\infty^2)} = 1.23 \times 10^{-2}, \tag{2.2}$$

where h is the width of the cavity nozzle exit.

No-stress boundary conditions are applied along the top and bottom of the wind tunnel, and no-slip boundary conditions are applied on the airfoil surface and cavity wall. Periodic boundary conditions are used along the spanwise (z) direction. At the exit boundary, the convective boundary condition is applied, with the convection speed determined by the streamwise velocity averaged across the exit plane.

2.2. *Grid spacing and resolution*

Two different meshes of 8 and 15 million cells and three different meshes of 8, 12, and 15 million cells are employed to examine grid resolution effect on LES solutions in the cases of angles of attack 16.6° and 20°, respectively. Grid lines are clustered around the nozzle of synthetic-jet actuator, blade boundary layer, and near wake to ensure appropriate resolution in important flow regions. A total of 24 and 30 mesh points are allocated along the cavity slot in the 8- and 15-million-cell meshes, respectively. The finer meshes were constructed by refining the 8-million-cell mesh especially in the boundary layer wall-normal direction and spanwise direction. Details of the grid spacing and resolution along the blade surfaces for the 15-million-cell mesh in the case of $\alpha = 16.6°$ are summarized in tables 1 and 2.

The simulation is advanced in time with the time step $\Delta t U_\infty / C = 1.7 \times 10^{-4}$ which corresponds to the Courant-Friedrichs-Lewy (CFL) number smaller than 1 in the most of the computational domain except for the region of synthetic-jet nozzle where the CFL number becomes up to 20. When the 15-million-cell mesh is employd, each time step requires a wallclock time of approximately 4.8 seconds when 200 CPUs of IBM P4 are used. The present results are obtained by integrating the governing equations over an interval of approximately $20C/U_\infty$.

x/C	$\Delta x/C$	Δx^+	$\Delta y/C$	Δy^+	Δz^+
0.1	2.84×10^{-4}	13.10	2.10×10^{-5}	0.49	96.07
0.3	1.93×10^{-3}	63.37	2.30×10^{-5}	0.38	68.40
0.5	3.00×10^{-3}	70.89	2.72×10^{-5}	0.32	49.20
0.7	3.17×10^{-3}	43.78	2.72×10^{-5}	0.19	28.76

TABLE 1. Grid spacing and resolution along the blade suction surface for the 15 million-cell mesh in the case of $\alpha = 16.6°$. $\Delta z/C = 2.08 \times 10^{-3}$.

x/C	$\Delta x/C$	Δx^+	$\Delta y/C$	Δy^+	Δz^+
0.1	2.70×10^{-3}	88.54	2.00×10^{-5}	0.33	68.21
0.3	4.06×10^{-3}	127.42	2.00×10^{-5}	0.31	65.23
0.5	4.47×10^{-3}	127.69	2.00×10^{-5}	0.29	59.38
0.7	4.04×10^{-3}	114.64	2.00×10^{-5}	0.28	59.08

TABLE 2. Grid spacing and resolution along the blade pressure surface for the 15-million-cell mesh in the case of $\alpha = 16.6°$. $\Delta z/C = 2.08 \times 10^{-3}$.
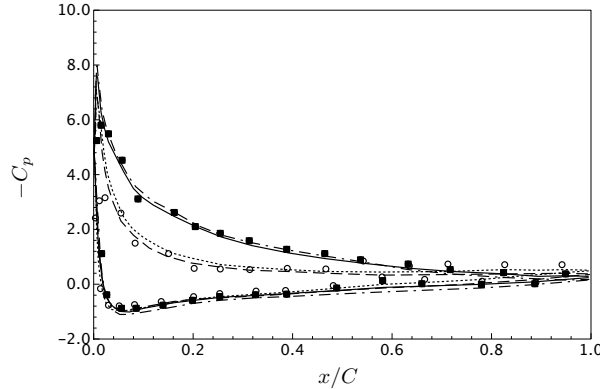

FIGURE 3. Mean pressure distribution over the airfoil surface at $\alpha = 16.6°$. ———— , controlled case on the 15-million-cell mesh; —·— , controlled case on the 8-million-cell mesh; ———— , uncontrolled case on the 15-million-cell mesh; ········ , uncontrolled case on the 8-million-cell mesh; symbols, experimental data of Gilarranz *et al.* (2005).

3. Results and discussion

Gross features of the flow over uncontrolled airfoils at $\alpha = 16.6°$ and $20°$ are revealed in figure 2, showing contours of the instantaneous streamwise velocity predicted by the present LES. The turbulent structures present over the suction surface qualitatively indicate the degree of flow separation. In the case of $\alpha = 16.6°$ (figure 2(a)), flow massively
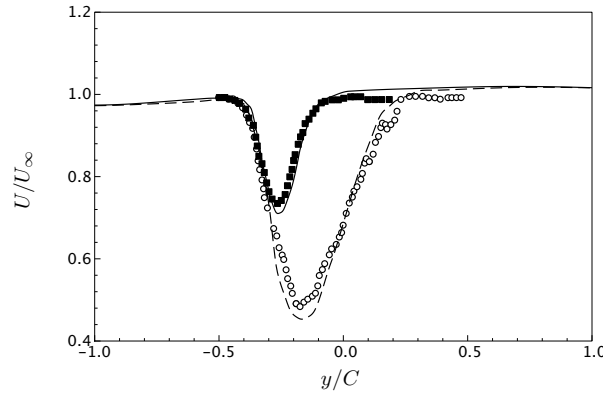
FIGURE 4. Mean streamwise velocity profiles at $x/C = 1.2$ in the case of $\alpha = 16.6°$. —— , controlled case; ---- , uncontrolled case; symbols, experimental data of Gilarranz *et al.* (2005). LES results on the 15-million-cell mesh are shown.

Case	Uncontrolled		Controlled	
	C_L	C_D	C_L	C_D
LES (8 million mesh)	0.83	0.28	1.43	0.23
LES (15 million mesh)	0.81	0.28	1.40	0.24
Experiment (Gilarranz *et al.* 2005)	0.82	0.26	1.41	0.22

TABLE 3. Summary of lift and drag coefficients in the case of $\alpha = 16.6°$.

separates from the half aft portion of the suction surface while flow separates from the leading edge in the $\alpha = 20°$ case (figure 2(*b*)). Qualitatively, these features are consistent with the experimental observation by Gilarranz *et al.* (2005).

The pressure distributions over the airfoil surfaces in both uncontrolled (---- , ········ , ○) and controlled (—— , —·— , ■) cases with two different grid resolution are compared with the experimental data in figure 3. In general, the present LES shows favorable agreement with experimental measurements in both cases. In addition, the effect of grid resolution on the pressure distribution is found to be not significant while LES solutions on a finer mesh (—— , ----) are slightly closer to the experimental data. The pressure distribution directly indicates the effect of synthetic jets on flow separation. Most of the lift enhancement is achieved in the upstream portion of the airfoil suction surface, while the control effect of synthetic jets on the pressure distribution in the pressure surface is negligible (see figure 3).

The lift and drag coefficients predicted by the present LES in the uncontrolled and controlled cases are in excellent agreement with the experimental data (Gilarranz *et al.* 2005) as shown in table 3. The present synthetic-jet actuation with the momentum coefficient of 1.23% produces more than a 70% increase in the lift coefficient. The drag coefficient is found to decrease approximately $15\% \sim 18\%$ with the synthetic-jet actuation.

The drag reduction due to the synthetic-jet actuation is also indicated by the wake profiles. Figure 4 shows the mean streamwise velocity profiles in the uncontrolled (----)
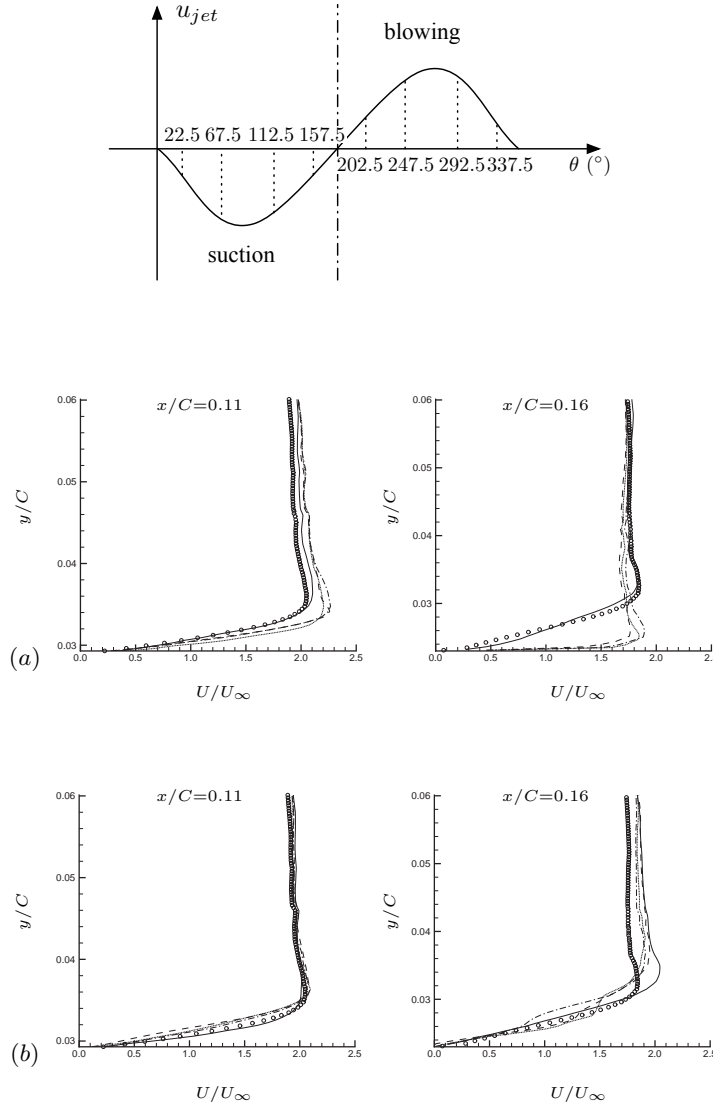
FIGURE 5. Profiles of the phase-averaged streamwise velocity in the case of $\alpha = 16.6°$. (a) Suction phase: ——— , $\theta = 22.5°$; – – – – , $67.5°$; ········ , $112.5°$; —·— , $157.5°$; (b) blowing phase: ——— , $\theta = 202.5°$; – – – – , $247.5°$; ········ , $292.5°$; —·— , $337.5°$. ∘ , uncontrolled case. The cavity slot is located at $x/C = 0.12$.

and controlled (———) cases in a downstream location at $x/C = 1.2$. The width of the wake and the peak magnitude of velocity deficit decrease with synthetic jet control. The present wake profiles are in favorable agreement with experimental data (Gilarranz *et al.* 2005) in both uncontrolled (∘) and controlled (∎) cases.

As shown in figure 5, in the case of $\alpha = 16.6°$, both the suction and blowing phases significantly modify the boundary layer on the suction surface of the airfoil. The synthetic-jet actuation not only stabilizes the boundary layer either by adding/removing the momentum to/from the boundary layer, but also enhances mixing between inner and outer
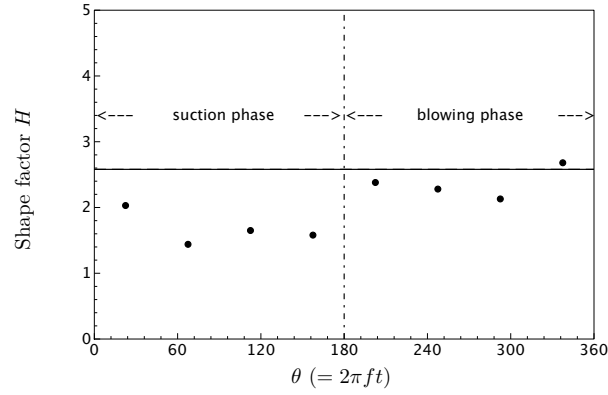
FIGURE 6. Shape factor (ratio of the displacement thickness to the momentum thickness) of the boundary layer at $x/C = 0.16$ in different phases shown in figure 5. ———— , shape factor in the uncontrolled case (2.58), ● , shape factor in the controlled case.
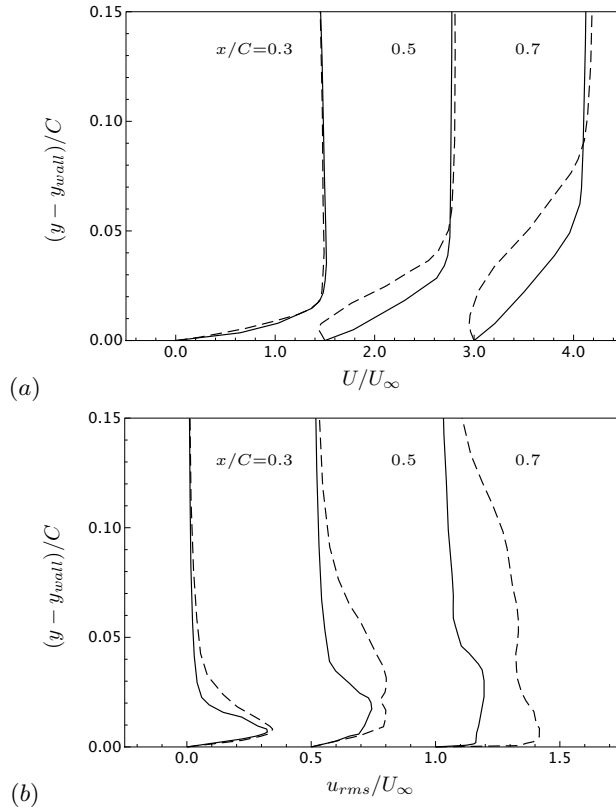

FIGURE 7. Profiles of (a) the mean streamwise velocity and (b) root-mean-squred streamwise velocity fluctuations at $x/C = 0.3$, 0.5, and 0.7 in the case of $\alpha = 16.6°$. ———— , controlled case; ――― , uncontrolled case. The profiles at $x/C = 0.5$ and 0.7 are shifted by 1.5 and 3 in (a) and 0.5 and 1 in (b), respectively. LES results on the 15-million-cell mesh are shown.
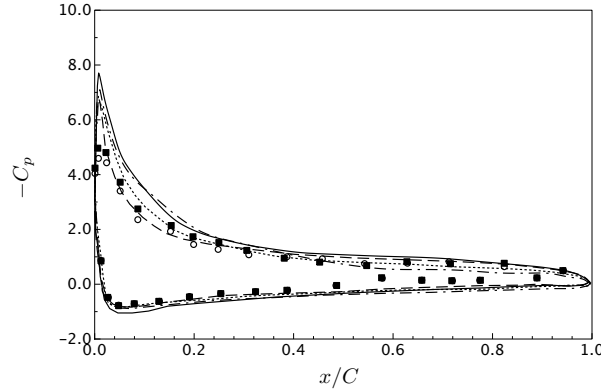
FIGURE 8. Mean pressure distribution over the airfoil surface at $\alpha = 20°$. ——— , controlled case on the 15-million-cell mesh; —·— , uncontrolled case on the 8-million-cell mesh; ········ , uncontrolled case on the 12-million-cell mesh; ---- , uncontrolled case on the 15-million-cell mesh; symbols, experimental data of Gilarranz *et al.* (2005).
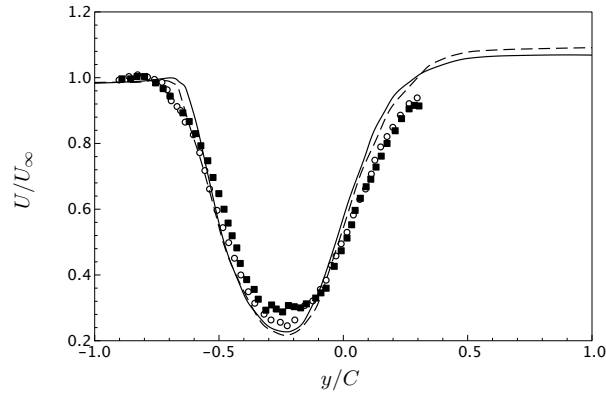

FIGURE 9. Mean streamwise velocity profiles at $x/C = 1.2$ in the case of $\alpha = 20°$. ——— , controlled case; ---- , uncontrolled case; symbols, experimental data of Gilarranz *et al.* (2005). LES results on the 15-million-cell mesh are shown.

parts of the boundary layer. The modification of the boundary layer in the upstream ($x/C = 0.11$) and downstream ($x/C = 0.16$) proximity to the exit slot of the synthetic-jet actuator ($x/C = 0.12$) is shown in figure 5. Compared to the velocity profile in the uncontrolled case (○), in the blowing phase (figure 5(b)), the downstream velocity profile becomes fuller due to additional momentum while the modification of the upstream velocity profile is not noticeable. On the other hand, in the suction phase (figure 5(a)), the low momentum flow in the boundary layer is removed and the thickness of the downstream boundary layer is significantly thinned. Therefore, the downstream flow separation is effectively prevented by the favorable modification of the blade boundary layer in both the blowing and suction phases.

The shape factors of the boundary layer which is defined as a ratio of the displacement thickness to the momentum thickness in different control phases are compared to the shape factor of the uncontrolled boundary layer at $x/C = 0.16$ (see figure 6). In general, a larger shape factor implies that the boundary layer is more prone to separation. As seen in figure 6, smaller shape factors compared to that in the uncontrolled cases are observed

Case	Uncontrolled		Controlled	
	C_L	C_D	C_L	C_D
LES (8 million mesh)	1.13	0.24		
LES (12 million mesh)	1.07	0.27		
LES (15 million mesh)	1.01	0.29	1.14	0.28
Experiment (Gilarranz *et al.* 2005)	0.94	0.31	1.03	0.30

TABLE 4. Summary of lift and drag coefficients in the case of $\alpha = 20°$.

in most of control phases. The reduction of the shape factor is especially significant in the suction phases. However, in the blowing phase $\theta = 337.5°$ in figure 5, the shape factor becomes slightly larger than that of uncontrolled case, and this imply the presence of intermittent separation even in the controlled case.

Figure 7 shows profiles of the mean streamwise velocity and root-mean-squared streamwise velocity fluctuations at three different streamwise locations $x/C = 0.3$, 0.5, and 0.7 in the case of $\alpha = 16.6°$. The mean velocity profile indicates that the boundary layer flow in the uncontrolled case (----) separates from the suctions surface around the mid-chord location while the boundary layer flow in the controlled case (——) does not separate from the suction surface even in the further downstream locations (figure 7(*a*)). Profiles of the root-mean-squared streamwise velocity fluctuations also indicates very different unsteady flow characteristics. The synthetic-jet actuation is found to effectively suppress turbulent fluctuations on the downstream boundary layer (——). In general, the wall-normal extent and magnitude of the turbulent fluctuations are much larger in the uncontrolled case (----) than in the controlled case (——) (figure 7(*b*)).

In the case of 20° angle of attack where flow separates near the leading edge, Figure 8 indicates that LES prediction is relatively sensitive to grid resolution. The leading-edge flow separation is found relatively difficult to predict since the accurate capture of the transition in the separated laminar shear layer is in general difficult to predict unless the mesh resolution is fine enough to capture the physics. It is found that LES provides comparable results to experimental data when grid resolution is sufficient to predict the separated shear layer (······ in figure 8). The synthetic-jet actuation at 12% chord location is found marginally effective in controlling leading edge separation. In the near wake at $x/C = 1.2$, the present LES shows a reasonable agreement with the experimental data and also indicates that the control effect is not noticeable. However, compared to the experimental data (Gilarranz *et al.* 2005), the synthetic-jet control is found to produce about 10% more lift coefficient in the present LES (see table 4).

4. Conclusions

Large-eddy simulations (LES) of turbulent flow separation over an airfoil with and without synthetic-jet control have been performed at two different stall conditions. To simulate detailed flow structures inside the synthetic jet actuator and the synthetic jet/cross flow interaction, an unstructured-grid finite-volume LES solver has been employed. Two flow configurations which consist of flow over a NACA 0015 airfoil at angles of attack 16.6° and 20° have been simulated at a Reynolds number of 896,000 based

on the airfoil chord length and freestream velocity. In the case of 16.6° angle of attack where flow separates around a mid-chord location, LES results show excellent agreement with experimental data for both uncontrolled and controlled cases. LES confirms the experimental finding that synthetic jets which are produced through a slot across the entire span on suction surface at 12% chord location, effectively delays the onset of flow separation and causes a significant increase in the lift coefficient. In the case of 20° angle of attack where flow separates near the leading edge, LES provides comparable results to experimental data when grid resolution is sufficient to predict the separated shear layer. The synthetic-jet actuation at 12% chord location is found marginally effective in controlling leading edge separation.

Acknowledgments

REFERENCES

GILARRANZ, J. L., TRAUB, L. W. & REDINIOTIS, O. K. 2005 A new class of synthetic jet actuators - part II: application to flow separation control. *Journal of Fluids Engineering* **127**, 377–387.

GLEZER, A. & AMITAY, M. 2002 Synthetic jets. *Annual Review of Fluid Mechanics* **34**, 503–529.

GRESHO, P. M. & LEE, R. L. 1981 Don't suppress wiggles - they're telling you something. *Computers and Fluids* **9**, 223–253.

KALTENBACH, H.-J. & CHOI, H. 1995 Large-eddy simulation of flow around an airfoil on a structured mesh. Annual Research Briefs, 51-60. Center for Turbulence Research, Stanford, California.

KHORRAMI, M. R., BERKMAN, M. E. & CHOUDHARI, M. 2000 Unsteady flow computations of a slat with blunt trailing edge. *AIAA Journal* **38** (11), 2050–2058.

KHORRAMI, M. R., SINGER, B. A. & RADEZTSKY, R. H. 1999 Reynolds-averaged navier-stokes computations of a flap-side-edge flowfield. *AIAA Journal* **37** (1), 14–22.

MATHIAS, D. L., ROTH, K. R., ROSS, J. C., ROGERS, S. E. & CUMMINGS, R. M. 1999 Navier-Stokes analysis of the flow about a flap edge. *Journal of aircraft* **36** (6), 833–838.

MITTAL, R. & MOIN, P. 1997 Suitability of upwind-biased schemes for large-eddy simulation of turbulent flows. *AIAA Journal* **36** (8), 1415–1417.

RUMSEY, C. L., GATSKI, T. B., SELLERS III, W. L., VATSA, V. N. & VIKEN, S. A. 2004 Summary of the 2004 CFD validation workshop on synthetic jets and turbulent separation control. *AIAA Paper 2004-2217.*

WYGNANSKI, I. 2004 The variables affecting the control of separation by periodic excitation. *AIAA Paper 2004-2505.*

YING, S. X., SPAID, F. W., MCGINLEY, C. B. & RUMSEY, C. L. 1998 Investigation of confluent boundary layers in high-lift flows. *Journal of aircraft* **35** (3), 550–562.

YOU, D. & MOIN, P. 2007 A dynamic global-coefficient subgrid-scale eddy-viscosity

model for large-eddy simulation in complex geometries. *Physics of Fluids* **19** (6), 065110.

You, D., Wang, M. & Moin, P. 2006 Large-eddy simulations of flow over a wall-mounted hump with separation control. *AIAA Journal* **44** (11), 2571–2577.